RSC Advances

ROYAL SOCIETY OF CHEMISTRY

www.rsc.org/advances

RSC Advances

ARTICLE

Fabrication of magnetically carbonaceous solid acids from banana peel for the esterification of oleic acid

Received 00th January 20xx,
Accepted 00th January 20xx

DOI: 10.1039/x0xx00000x

www.rsc.org/

Rui-Lin Liu [a, b*], Xiang-Yu Gao [a], Lei An [a], Jin Ma [a], Ji-Fang Zhang [a] and Zhi-Qi Zhang [a*]

Magnetic carbonaceous solid acids (MCSAs), which are important materials with many practical and research applications, have recently attracted much attention. In this work, a kind of valuable MCSAs with superparamagnetism were synthesized by using a facile strategy, i.e., integrated fast pyrolysis of Fe(III)-based complexes and vapor-phase sulfonation from waste banana peel (BP). This versatile strategy enables simple preparation of MCSAs with easily tunable surface areas (156–1097 $m^2 g^{-1}$) and pore volumes (0.17–0.74 $cm^3 g^{-1}$), and relatively large average mesoporous sizes (6.1–11.4 nm), by simply varying the dosage of Fe(III) ions. The as-prepared MCSAs have excellent catalytic activities in the esterification of oleic acid with methanol, far higher than those of commercial Amberlyst-15, sulfonated activated carbon, and niobic acid, under the same conditions. In particular, the catalytic activities of the obtained MCSAs rival that of a homogeneous H_2SO_4 catalyst. The present work provides an inexpensive and environmentally friendly method to synthesize MCSAs from waste BP and may contribute to a holistic approach for biomass conversion.

1. Introduction

Biodiesel is a sustainable, biodegradable and non-toxic diesel fuel substitute that is widely used worldwide.[1] It can be made from vegetable oils, animal fats, and waste oils from the food industry.[2,3] Biodiesel can be easily produced by catalytic transesterification of triglycerides with alcohols or catalytic esterification of free fatty acids (FFAs) in the presence of base or acid catalysts.[4] However, when the raw materials contain a high percentage of FFAs, alkaline catalysts react with the FFAs to form soaps. This reaction not only consumes the catalyst, but also reduces the yield of the biodiesel product;[3] this makes the purification of biodiesels extremely difficult.[5] In such cases, an acid catalyst is preferable, because it can reduce saponification. Compared with homogeneous acid catalysts, heterogeneous solid acid catalysts (HSACs) are preferred, because they are greener and recyclable, and many types of HSACs have been successfully developed for FFA esterification with methanol.[2,6] However, the reported HSACs for FFA esterification are unsatisfactory, because of the low densities and low accessibility of the acid sites, easy deactivation, and high cost;[7,8] these factors hinder their use in large-scale production. It is therefore still necessary to develop simple, low-cost, and green methods for synthesizing novel HSACs for biodiesel production.

Compared with conventional HSACs, magnetic solid acid can be easily separated in the presence of external magnetic fields, particularly in viscous or solid reaction mixtures.[9] Lately, a series of magnetic solid acids were synthesized by sulfonation of a series of particles consisting of Fe_3O_4 cores with various shell materials.[2,10,11] However, many of the reported magnetic solid acids are unsatisfactory in acid-catalyzed reactions.[9,10] Additionally, the preparation of these magnetic solid acids involves complex synthetic procedures, and often requires expensive or toxic reagents,[9] impeding large-scale production.

Carbon-based solid acid (CSA) is ideal for esterification reactions owing to such advantages as chemical inertness, mechanical stability, structural diversity and surface hydrophobicity.[12] Study results indicate that the catalytic activity of a CSA is highly dependent upon the starting materials.[13] However, most studies have focused mainly on a limited number of feedstocks, especially pure carbohydrates, such as glucose, starch, sucrose, and cellulose.[1] Additionally, conventional preparation methods for magnetic CSA are highly complex. A magnetic core is firstly fabricated, followed by coating with a shell with a porous carbon layer, and sulfonation of the magnetic carbon. Thus, it is of great interest to synthesize magnetic CSA by a low-cost precursor and facile route as well as to investigate their structure and property.

Banana is a worldwide consumed tropical fruit. BP is the main residue, and has been mainly used in composting, animal feeding, and the production of proteins, ethanol, methane, pectin, and enzymes.[14] Especially, BP is rich in a variety of functional groups, including carboxyl, hydroxyl, and amide groups, and can be easily modified and assembled using metal ions.[15] Thus, it is highly desirable to develop green and economical ways to deal with waste

[a] Key Laboratory of Analytical Chemistry for Life Science of Shaanxi Province, School of Chemistry and Chemical Engineering, Shaanxi Normal University, Xi'an 710062, PR China.
[b] School of Pharmacy, Xi'an Jiaotong University, Xi'an 710061, PR China.
E-mail: zqzhang@snnu.edu.cn (Z.-Q. Zhang) & lrlsxsd@snnu.edu.cn (R.-L. Liu).
Electronic Supplementary Information (ESI) available: [details of any supplementary information available should be included here]. See DOI: 10.1039/x0xx00000x

BP, as well as to utilize the wastes to produce staple or value-added products.

Herein, a facile strategy for the fabrication of magnetic CSAs was developed by using waste BP as a precursor, involving pyrolysis of Fe(III)-based complexes followed by vapor-phase sulfonation. This process not only provides magnetic CSAs, but also produces bio-oil, which can be used for fuel and chemical production.[16] To obtain highly porous magnetic CSA supports, the influence of the Fe(III) ion concentration was assessed. The catalytic activities of the as-made materials were investigated by esterification of oleic acid (OA) with methanol. The physical and chemical properties of the as-made materials were also characterized in detail, and its structure-function relationship was investigated with Fourier transform infrared spectroscopy (FTIR), Thermal gravimetric analysis (TGA), X-ray diffraction (XRD), Scanning electron microscopy (SEM), Transmission electron microscopic (TEM), X-ray photoelectron spectroscopy and others.

2. Experimental

2.1 Fabrication of the magnetic porous carbons (MPCs)

Briefly, BP fragments (1.2 kg) were completely submerged in an aqueous $FeCl_3$ solution (1.8 L) of a certain concentration for 1 week at 80 °C. In this process, the –COOH and –OH groups on the BP pore surfaces easily coordinated with adsorbed Fe ions, as the solvent gradually evaporated, and gray-black Fe-based composites were obtained after drying at 100 °C. The Fe-based composites were carbonized at 650 °C at a heating rate of 1 °C min^{-1} for 3 h under nitrogen. The volatiles produced during pyrolysis were swept out by a nitrogen flow of 300 mL min^{-1}, and condensed with cold ethanol to give a bio-oil. The resultant black monoliths were smashed, washed with deionized water and anhydrous ethanol to remove uncoordinated Fe ions and organic impurities, and dried at 100 °C for 24 h, to give magnetic porous materials (**Fig. S1**). The as-synthesized samples were designated MPC-*x*, where *x* indicates the concentration (M) of the $FeCl_3$ solution. For comparison of the physical characteristics, another carbon material was synthesized by direct pyrolysis of BP (DPBP) under the same conditions.

2.2 Synthesis of MPCs-x-SO_3H catalysts

The sulfonation of MPC-*x* were completed by the method of vapor-phase sulfonation[10] with slight modification. Briefly, the MPC-*x* were sulfonated by using fuming sulfuric acid (10 mL of fuming sulfuric acid to 1 g of solid MPC-*x*) at 393 K for 8 h in a Teflon-lined autoclave. After sulfonation the mixture was cooled to room temperature, and then added to a beaker containing deionized water. Subsequently, the suspension was filtered, washed with deionized water until the pH of wash water was about 7-8 and dried at 80 °C for 4 h. After that, the samples were magnetic attracted with external magnet and used for further use (Fig. S1). For comparison of the catalytic properties, DPBP and activated carbon (AC) were sulfonated by using the same method; which were denoted by DPBP-SO_3H and AC-SO_3H, respectively.

2.3 Esterification of OA with methanol

Liquid-phase esterification of OA with methanol, which was used as the model reaction, was performed in a three-necked round-bottomed flask connected to a water-cooled condenser. Briefly, OA (0.15 g) was introduced into the flask, and the temperature was increased to 80 °C. After the OA had melted, warm methanol (5 g) and the catalyst (0.15 g) were quickly added, and the mixture was mechanically stirred and kept at 80 °C for 8 h in an oil bath. The weight ratio of OA to methanol was 1:33, and the concentration of the catalyst in the reaction solution was 3 wt%. After reaction for the specified time interval, the catalyst was separated from the mixture using a permanent magnet, and the collected mixture (200–600 μL) was filtered through a membrane (pore size 0.22 μm). Aliquots (200 μL) of the resulting solution were withdrawn and kept for 10 min at 70 °C under vacuum to remove methanol, followed by addition of anhydrous *n*-hexane (200 μL) containing methyl palmitate (10 mg mL^{-1}, as an internal standard). Gas chromatography was performed using a Shimadzu 2010 instrument equipped with a flame ionization detector and poly(ethylene glycol) capillary column (30 m × 0.25 mm × 0.25 μm). The performances of the MPCs-*x*-SO_3H catalysts were compared with those of H_2SO_4 (0.15 g), Amberlyst-15 (0.15 g), and niobic acid (0.15 g).

The catalytic activities were evaluated based on the yields of methyl oleate, *Y* (%) and reaction turnover frequencies (TOFs) (min^{-1}). *Y* (%) is calculated as follows:

$$Y = \sum \text{yield}_{\text{esters}} = \frac{\sum f_{\text{ester}} A_{\text{ester}} \times m_{\text{internal}}}{A_{\text{internal}} \times m_{\text{esters}}} \times 100\% \qquad (1)$$

Where A_{ester} is the peak area of fatty acid methyl esters, A_{internal} is the peak area of internal standard, m_{internal} is the mass of internal standard, m_{esters} is the mass of fatty acid methyl esters and f_{ester} is the correction factor of the main fatty acid methyl esters.

The TOFs for OA esterification were calculated from the amounts of methyl oleate formed, under the initial reaction rate within 2 h. The TOF value is obtained by equation (2):[3]

$$\text{TOF} = \frac{M_O}{\varphi M_{AS}} \qquad (2)$$

where M_O is the number of moles of methyl oleate produced in reaction time φ, and M_{AS} is the number of moles of acid sites, determined by ion-exchange titration.

3. Results and discussion

3.1 Characterization of magnetic CSAs

The treatment of BP with different concentrations of Fe(III) under the same conditions gave different textures. SEM images show that MPC-0.4 and MPC-0.4-SO_3H, and MPC-0.8 and MPC-0.8-SO_3H have distinctly porous or nanosheet-like textures (Fig. 1). Other materials, prepared using different Fe(III) concentrations (0.2, 0.6, and 1.0 M) also had clearly porous frameworks (Fig. S2, S3). It is worth noting, however, that the porous structure of MPC-*x* became increasingly developed with increasing Fe(III) concentration from 0.2 to 1.0 M to give a good porous framework for catalyst support. This is conducive to provide a fast mass transfer pathway through the mesostructure of the catalyst supports. The MPC-*x*-SO_3H catalysts

had slightly more abundant pores than the MPC-*x* catalysts under the same conditions; this could be ascribed to partial corrosion or etching of the magnetic iron oxide matrix. In contrast, the raw BP has no obviously porous texture (Fig. S3).

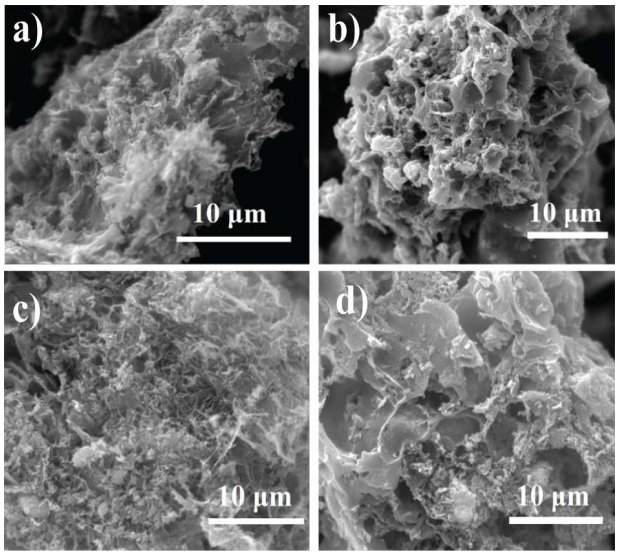

Fig. 1. SEM images of (a) MPC-0.4, (b) MPC-0.4-SO_3H, (c) MPC-0.8, and (d) MPC-0.8-SO_3H

The crystal structures of the as-obtained materials were determined using XRD. As shown in Fig. 2(a), the XRD pattern of MPC-1.0, used as an example, has strong and broad diffraction peaks of 2θ ≈ 20° and 26°, which can be attributed to amorphous carbon composed of randomly oriented aromatic carbon sheets[17] and the (002) diffraction peak of graphitized carbon,[15] respectively. The XRD peaks at 2θ = 30.2°, 35.6°, 36.6°, 43.2°, 54.8°, 57.1°, 62.7°, and 74.6° indicate the formation of Fe_3O_4 crystallites during fast pyrolysis, in good agreement with the standard literature data (JCPDS card No. 79-0417). The XRD patterns of the other samples show that they contain carbon and Fe_3O_4 (Fig. S4). This means that the products are in the form of carbon–Fe_3O_4 nanocomposites. The XRD patterns of MPC-1.0-SO_3H and the other MPC-*x*-SO_3H samples indicate that Fe_3O_4 could survive after vapor-phase sulfonation (Fig. S4). Energy dispersive X-ray (EDX) shows that the MPC-*x* and MPC-*x*-SO_3H surfaces are composed mainly of C, O, and Fe elements (Fig. S5).

Raman spectra of the MPC-0.4 and MPC-0.4-SO_3H samples (Fig. 2b) have a distinct pair of broad bands, at 1340 (D band) and 1584 cm^{-1} (G band). The D band is associated with disorder, allowing the zone edge modes of the graphite structure to become active as a result of lack of long-range order in the amorphous and quasi-crystalline forms of carbon materials.[10] The G band corresponds to the E_{2g} mode in the basal plane of crystalline graphite.[18] The peak intensity ratio of the D and G bands (I_D/I_G) generally provides a useful index for comparing the degrees of crystallinity of carbon materials: the smaller the value of I_D/I_G is, the higher the degree of ordering in the carbon material.[18] All of the samples have similar Raman spectra, but their I_D/I_G ratios vary slightly (Fig. 2b and Fig. S6). The I_D/I_G value of MPC-*x*-SO_3H is slightly higher than that of MPC-*x*, suggesting that the incorporation of sulfonic acid groups reduces the average size of the sp^2 carbon domains.[19]

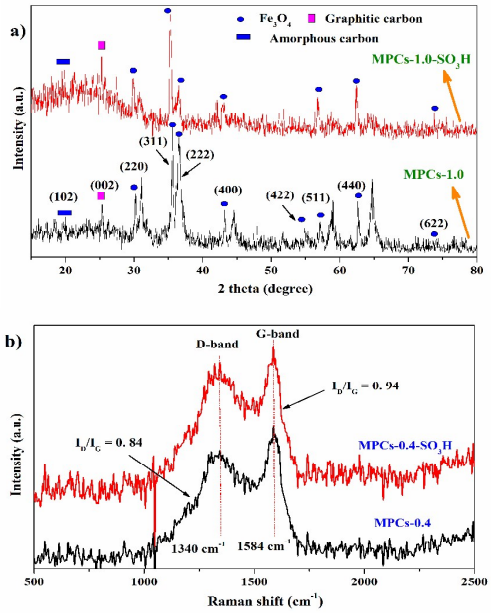

Fig. 2. XRD patterns of MPCs-1.0 and MPCs-1.0-SO_3H (a), and raman spectra of MPCs-0.4 and MPCs-0.4-SO_3H (b)

TEM images show that MPC-0.4 has wire-like or nanosheet-like microstructures (Fig. 3a). The TEM images of MPC-0.4 and MPC-0.4-SO_3H clearly show that well-crystallized Fe_3O_4 nanoparticles are distributed in the surface of the amorphous carbon matrix (Fig. 3b–f). Furthermore, close observation of the TEM images shows that iron oxide nanoparticles in the obtained composites have a unique semi-exposed morphology, with one part of the nanoparticle partially exposed to the pore channels and the other part tightly trapped in the carbon framework (Fig. 3c, f). These clearly confirm that part of Fe_3O_4 nanoparticles are effectively incorporated into the carbon framework, and the embedded Fe_3O_4 nanocrystals have a grain size range of 5–8 nm (Fig. 3f). Careful examination of the corresponding high-resolution TEM image shows well-resolved lattice fringes with an interplanar distance of 0.25 nm, from the (311) plane of Fe_3O_4,[18] in the MPC-0.4-SO_3H sample (Fig. 3g). The other samples also have similar characteristics (Fig. S7–S10). To obtain further insights into the nanoparticle locations in the carbon matrix, the Fe_3O_4 particles were removed from the MPC-0.4-SO_3H sample by soaking in dilute HCl solution; a large number of honeycomb-like nanopores remained (Fig. 3h). The result fully confirms that the carbon matrix efficiently prevents the Fe_3O_4 nanoparticles from leaching out and aggregating during the oxidation treatment, i.e., most of Fe_3O_4 nanoparticles are wrapped with carbon layers. It was found that the porous carbon layer on the surface of Fe_3O_4 cores can not only stabilize the Fe_3O_4 against aggregation and prevent oxidation of Fe_3O_4, but also can be coordinated or grafted with –SO_3H groups as a Brønsted acid for many practical applications in the chemical industry.[9,10] In contrast, neither wire-like nor porous structures are detected in the SEM and TEM images of DPBP-SO_3H and DPBP (Fig. S3e–h and Fig. S10f–h). TGA was used to determine the chemical composition of the MPC-

x-SO_3H samples, at a heating rate of 10 °C min^{-1} in an air atmosphere. The sample was heated to 650 °C, so that Fe_3O_4 was oxidized to Fe_2O_3 and carbon was oxidized to carbon dioxide. Based on the remaining weight (of Fe_2O_3), the amount of Fe_3O_4 was calculated to be between 7.54 and 21.46 wt% after sulfonation (Fig. S11).

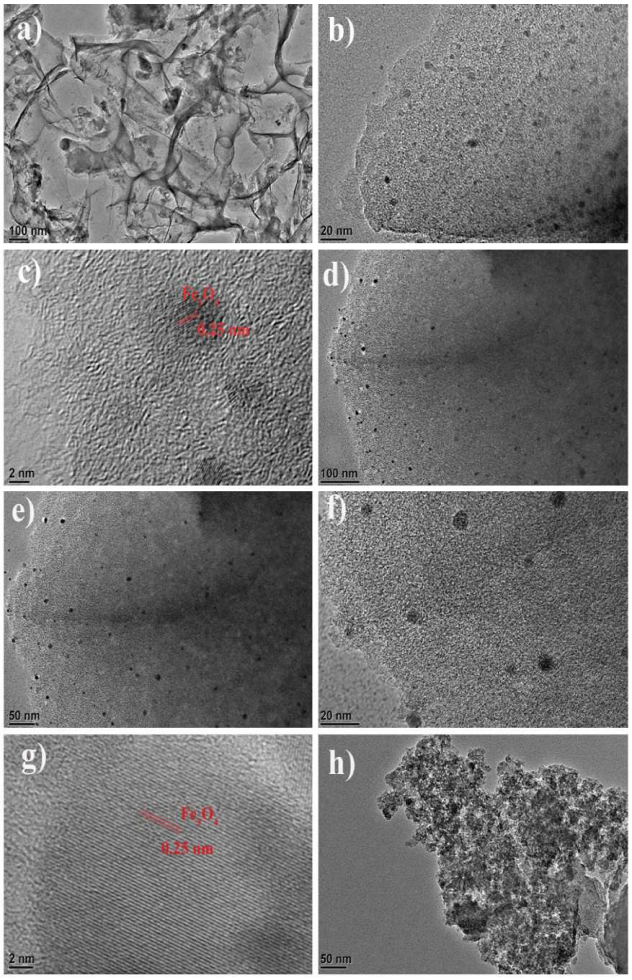

Fig. 3. TEM images of (a–c) MPC-0.4, (d–f) MPC-0.4-SO_3H, (g) high-resolution TEM image of Fe_3O_4 nanoparticle in (f), and (h) MPC-0.4-SO_3H after treatment with dilute HCl solution, at different magnifications

As shown in Fig. 4a, XPS of MPC-0.6, MPC-0.6-SO_3H, and DPBP-SO_3H clearly reveals six peaks, from Si2p (103.4 eV), S2p (169.5 eV), C1s (284.5 eV), N1s (400.4 eV), O1s (531.6 eV), and Fe2p (713.5 eV).[9,20] For comparison, the Fe2p peaks in the MPC-0.6 and MPC-0.6-SO_3H spectra, and the S2p peaks in the MPC-0.6-SO_3H and DPBP-SO_3H were examined. The C1s spectrum of MPC-0.6-SO_3H includes four peaks, with binding energies that can be differentiated via deconvolution (Fig. 4b). These peaks can be assigned to the carbon atoms in C–S (283.9 eV), C=C/C–C (284.5 eV), C–O (phenolic hydroxyl and/or ether, 285.4 eV), and C=O (carbonyl and/or quinine, 286.5 eV) functional groups.[9,21,22] In contrast, the C1s spectrum of MPC-0.6 prior to sulfonation does not contain carbon atoms in the form of C–S (Fig. S12). To further validate this result, the S2p spectrum (Fig. 4c) of MPC-0.6-SO_3H was deconvoluted into several single peaks, which correspond to S–C (168.1 eV), S–O (166.9 and 169.0 eV), and S=O (169.9 eV) bonds;[9,10,23] these are consistent with the FTIR spectra (Fig. S13) and further verify the presence of SO_3H groups. The O1s spectra of MPC-0.6 and MPC-0.6-SO_3H show the presence of Fe–O and C–O–Fe groups (Fig. S12, S14), suggesting linkage of Fe_3O_4 with porous carbon through this bond.

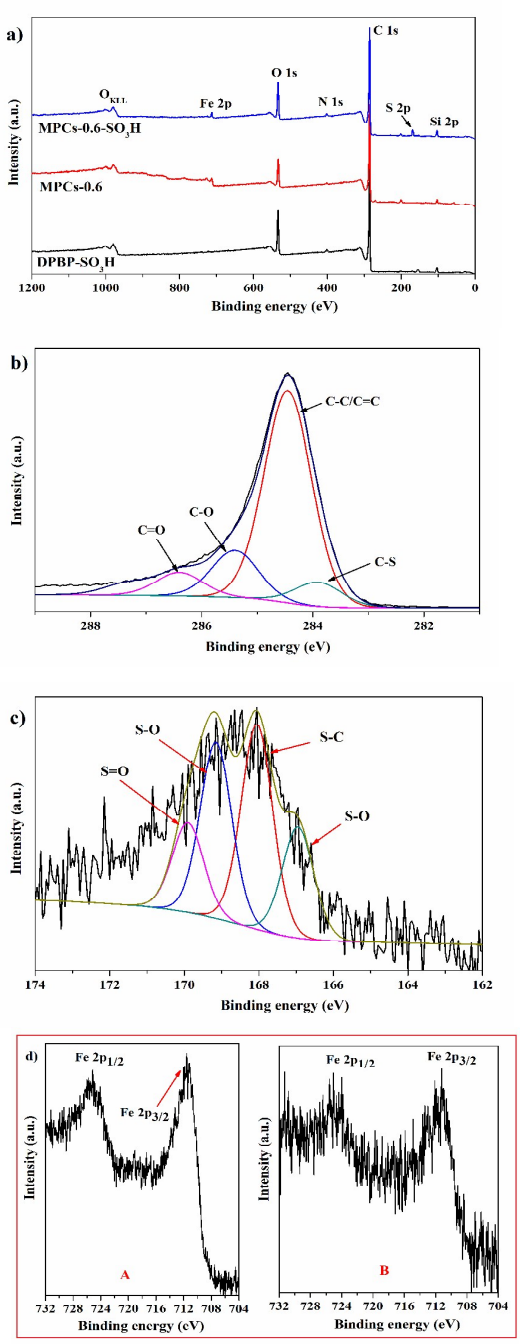

Fig. 4. XPS spectra of MPC-0.6, MPC-0.6-SO_3H, and DCBP-SO_3H: (a) survey spectrum of three carbons, (b) C1s spectrum of MPC-0.6-SO_3H, (c) S2p spectrum of MPC-0.6-SO_3H, (d) Fe2p spectra of MPC-0.6 (image A) and MPC-0.6-SO_3H (image B)

The XRD patterns of Fe_3O_4 and γ-Fe_2O_3 nanoparticles are similar; therefore MPC-0.6 and MPC-0.6-SO_3H were further identified by XPS. The Fe2p high-resolution XPS pattern in Fig. 4d shows that the binding energy values of Fe2p3/2 and Fe2p1/2 are 711.3 and 725.0 eV, respectively, consistent with previous reports on Fe_3O_4 nanoparticles.[24] Furthermore, the absence of an obvious satellite at 719.0 eV indicates that the MPC-*x* samples contain Fe_3O_4 rather than γ-Fe_2O_3, which is consistent with the XRD results. The present result is very similar with the sulfonation of magnetic carbon with sulfuric acid.[10] In addition, the densities and distributions of the C, O, S, and Fe elements in MPC-0.6-SO_3H were evaluated using XPS microarea mapping (Fig. S15). S is homogeneously distributed over the entire surface of MPC-0.6-SO_3H, suggesting effective sulfonation of the magnetic carbonaceous precursor. Fe is also homogeneously distributed over the entire surface of MPC-0.6-SO_3H, which is consistent with the TEM and EDX results. The C1s and S2p spectra of DPBP-SO_3H show that the –SO_3H group was successfully grafted onto the DPBP surface by sulfonation (Fig. S14). Compared with those in MPC-0.6-SO_3H, the density and distribution of S in DPBP-SO_3H is very sparse.

The nitrogen sorption isotherms of the MPC-*x* and MPC-*x*-SO_3H samples (Fig. S16-S18) exhibit combined type I and type IV isotherm characteristics,[20] with a steep increase at low relative pressure, suggesting microporous characteristics. Additionally, the broad hysteresis loop in the medium relative pressure range indicates the presence of interstitial porosity. Results show that the surface areas and total pore volumes of the MPC-*x* samples are higher than those of DPBP (Table S1). This means that the Fe-based composite acts as a self-supporting template, which can enhance the formation of porous structures during biomass carbonization, mainly because the dehydration and decomposition of the Fe-based composite promotes the release of volatile matter during biomass pyrolysis; this increases the surface area and pore volume. Similar phenomena have been observed in the carbonization of Fe-based metal–organic frameworks.[25,26] The residual Fe can also catalyze the formation of porous structures during carbonization. This phenomenon has also been observed in the carbonization of $FeCl_3$-impregnated pinewood sawdust and polymer/biomass composites.[9] However, the main contribution to the surface area comes from the carbon support structure.[26] The effect on pore formation of varying the Fe(III) concentration was investigated, for magnetic carbons produced at Fe(III) concentrations of 0.2–1.0 M. As *x* changes from 0.2 to 1.0, the BET surface area and total pore volume of MPC-*x* first increase from 180–505 $m^2\ g^{-1}$ and 0.19–0.39 $cm^3\ g^{-1}$, respectively, and then decrease and retain to about 380 $m^2\ g^{-1}$ and 0.35 $cm^3\ g^{-1}$ accordingly. The average mesoporous size, between 6.15 and 11.38 nm (Table S1), is in the large nanoscale range. The surface areas and pore volumes of MPC-0.2-SO_3H and MPC-0.4-SO_3H are 156.7 $m^2\ g^{-1}$ and 0.17 $cm^3\ g^{-1}$, and 173.2 $m^2\ g^{-1}$ and 0.26 $cm^3\ g^{-1}$, respectively, which are significantly lower than those of MPC-0.2 (180.7 $m^2\ g^{-1}$ and 0.19 $cm^3\ g^{-1}$) and MPC-0.4 (505.1 $m^2\ g^{-1}$ and 0.39 $cm^3\ g^{-1}$). These results suggest that the MPC porous structure was partly damaged by sulfonation, and also indicates successful grafting of –SO_3H functional groups.[10] However, the surfaces area and pore volumes of MPC-0.6-SO_3H, MPC-0.8-SO_3H, and MPC-1.0-SO_3H are clearly higher than those of MPC-0.6, MPC-0.8, and MPC-1.0, respectively. This can be mainly ascribed to corrosion of some of the Fe_3O_4 nanoparticles during sulfonation. The average PSDs show that the average pore sizes of all the sulfonated MPC-*x* samples were between 2.35 and 3.58 nm (Fig. S16, Table S1, Fig. S17, S18). These findings reveal that the vast majority of the pores fell in the mesoporous range for MPC-*x*-SO_3H, whereas DPBP-SO_3H and AC-SO_3H contain only micropores (Table S1). Overall, the results show that this versatile strategy not only gives materials with high BET surface areas and large pore volume, but also provides preferable stability under high temperature and hydrolytic conditions for MPC-*x*-SO_3H (Fig. S19).

Synthesis of MPC precursor materials is the primary step for MPC-*x*-SO_3H synthesis, which includes the following steps (Fig. S20): It is known that BP is composed of biopolymers in plant cell walls, such as celluloses, hemicelluloses, pectins, lignins, and proteins.[15] The –COOH and –OH groups on the surfaces of BP pores therefore easily coordinate with adsorbed Fe(III) ions, with gradual evaporation of the solvent, giving grey-black Fe(III)-based complexes; these are similar to metal–organic frameworks. The Fe(III)-based complexes were used as self-supporting templates and converted by simultaneous pyrolysis and nucleation to Fe_3O_4/C nanocrystalline frameworks with different porous structures (i.e., MPC-*x* materials). The Fe preloaded on the biomass in the form of $FeCl_3$ is also partly hydrolyzed to FeO(OH) during drying (equations 3 and 4). These FeO(OH) species were wrapped in BP. Additionally, the FeO(OH) was reduced to Fe_3O_4 at 650 °C by reducing components such as H_2, CO, and amorphous carbon, which were formed in the carbonation process (equations 5–7).[9]

$$FeCl_3 + 3H_2O \rightarrow Fe(OH)_3 + 3HCl\uparrow \quad (3)$$

$$Fe(OH)_3 \rightarrow FeO(OH) + H_2O \quad (4)$$

$$6FeO(OH) + 4H_2 \rightarrow 2Fe_3O_4 + 4H_2O\uparrow \quad (5)$$

$$6FeO(OH) + 4C \rightarrow 2Fe_3O_4 + 2CO\uparrow \quad (6)$$

$$6FeO(OH) + 4CO \rightarrow 2Fe_3O_4 + 4CO_2\uparrow \quad (7)$$

Furthermore, $FeCl_3$ easily dehydrates carbohydrate polymers at high temperatures and can change the decomposition pathway of lignocellulosic biomass during fast pyrolysis, inhibiting the formation of heavy tars, which can block porous structures, thus improving the formation of open pores in the carbon matrix. Meanwhile, the formed Fe species, i.e., FeO(OH) and Fe_3O_4, may act as in situ catalysts in fast pyrolysis, generating porous structures and favoring the formation of a dense layer-like "Fe template", which limits the growth of carbon atoms along the two-dimensional plane.[27] Overall, the BP first experiences simultaneous adsorption/coordination and hydrolysis to a Fe-based composite, and then undergoes pyrolysis and sulfonation to produce MPC-*x*-SO_3H.

3.2 Acid site density

It has been reported that –SO_3H functional groups can be added to a catalyst surface by vapor-phase sulfonation.[10] The results are shown in Table 1. MPC-0.4-SO_3H has a significantly larger acid site density than MPC-1.0-SO_3H, although the BET surface area of MPC-1.0-SO_3H is four times that of MPC-0.4-SO_3H; the acid site density of

MPC-0.4-SO_3H is twice that of MPC-1.0-SO_3H, which is opposite of the surface area trend. This is probably because sulfonation increases the BET surface area of MPC-1.0, by etching the Fe_3O_4 nanoparticles or opening small pores, which causes a decline in the H_2SO_4 concentration. The low concentration of H_2SO_4 weakens sulfonation of the MPC-1.0 surface. The acid-exchange capacities of the other MPC-*x*-SO_3H samples were above 1.70 mmol H^+ g^{-1}, and even reached 2.68 mmol H^+ g^{-1} for MPC-0.8-SO_3H; this value is higher than those of most other sulfonic acid-functionalized mesoporous materials reported so far.[19,28,29]

The XPS results indicate that the S in MPC-*x*-SO_3H is mainly associated with SO_3H groups, so the SO_3H contents of MPC-*x*-SO_3H can be estimated from the S contents. The S contents of MPC-0.6-SO_3H and DPBP-SO_3H are 4.8 and 0.9 wt%, respectively; which are very close to the results of elemental analyses (Table S1). The SO_3H contents of MPC-0.6-SO_3H and DPBP-SO_3H are therefore calculated to be 1.59 and 0.28 mmol g^{-1}, respectively. The total concentrations of acid sites on MPC-0.6-SO_3H and DPBP-SO_3H are 2.47 and 0.58 mmol g^{-1}, respectively, determined by titration with NaOH solution. The larger contents of acid sites compared with those of SO_3H in the solid acid suggest that acid groups other than SO_3H groups, such as COOH, are also present in the solid acid.[9] This was confirmed by XPS and FTIR (Fig. 4, Fig. S13).

NH_3-TPD was employed as a qualitative probe for determining the strength of acid site. The NH_3-TPD profiles of the MPC-0.6-SO_3H and MPC-0.8-SO_3H calcined at various temperatures are typically measured (data not shown). The NH_3-TPD profiles showed that all the catalysts had two distinct desorption peaks from 230 to 300 °C and 500 to 700 °C that were assigned to two types of acid sites. The low and high temperature peaks corresponded to weak and strong acid sites, respectively. In general, it can be expected to give a higher activity for the production of biodiesel from FFA because it has more acid sites and stronger acidity.

3.3 Catalytic activities for esterification of OA

The methyl oleate yields as a function of reaction time are shown in Fig. 5(a). The values of the maximum yields obtained in 8 h using the solid catalysts are shown in Table 1. It can be clearly seen that MPC-0.8-SO_3H gives the best catalytic activity. Based on the yields, the order of the catalytic activities of the solid catalysts is MPC-0.8-SO_3H > MPC-0.2-SO_3H > MPC-0.6-SO_3H > MPC-0.4-SO_3H = Amberlyst-15 > MPC-1.0-SO_3H > AC-SO_3H > DPBP-SO_3H > niobic acid. It is worth pointing out that the catalytic activities of MPC-0.2-SO_3H (90.3% conversion) and MPC-0.8-SO_3H (94% conversion) are comparable to that of H_2SO_4 (99% conversion) when the reaction time is 8 h.

The initial rates and TOFs of these solid catalysts are shown in Table 1. It should be noted that the initial rates and TOFs of MPC-0.2-SO_3H and MPC-0.8-SO_3H are significantly higher than those of Amberlyst 15. Additionally, the initial rates and TOFs of the other MPC-*x*-SO_3H catalysts are significantly higher than those of AC-SO_3H, DPBP-SO_3H, and niobic acid. It can be seen that the MPC-*x*-SO_3H catalysts are superior to Amberlyst-15 and niobic acid. It has been reported that the hydrophobicity around the acid sites is an important factor in achieving high catalytic activity.[3] The acid sites located on hydrophobic carbonaceous surfaces should therefore play a critical role in the high initial rates and TOFs of the present solid catalysts, because they enable effective adsorption of long-chain fatty acid molecules and removal of the water, especially in the early stage. The increase in the reactant concentration on the catalyst leads to enhancement of the activity, in good agreement with the reactant enrichment in carbon nanotube catalysts.[30]

Pore size is another significant issue for solid acids in esterification reaction. Although both the surface area and amount of acid sites of the MPC-0.2-SO_3H catalyst are lower than those of MPC-0.4-SO_3H, the initial methyl oleate formation rate and final conversion by MPC-0.2-SO_3H, which has larger mesopores (11.4 nm), are higher than those by MPC-0.4-SO_3H (9.4 nm). Similarly, the surface area and amount of acid sites of MPC-0.6-SO_3H are very similar to those of MPC-0.8-SO_3H, but the initial methyl oleate formation rate and final conversion by MPC-0.8-SO_3H, which has larger pores (8.8 nm), are clearly higher than those of MPC-0.6-SO_3H (6.0 nm). The effect of pore size on the catalytic activity demonstrates that factors favoring diffusion of large organic molecules contribute to enhancement of the catalytic properties, similar to the sulfonated ordered mesoporous carbon in the catalytic preparation of biodiesel.[28]

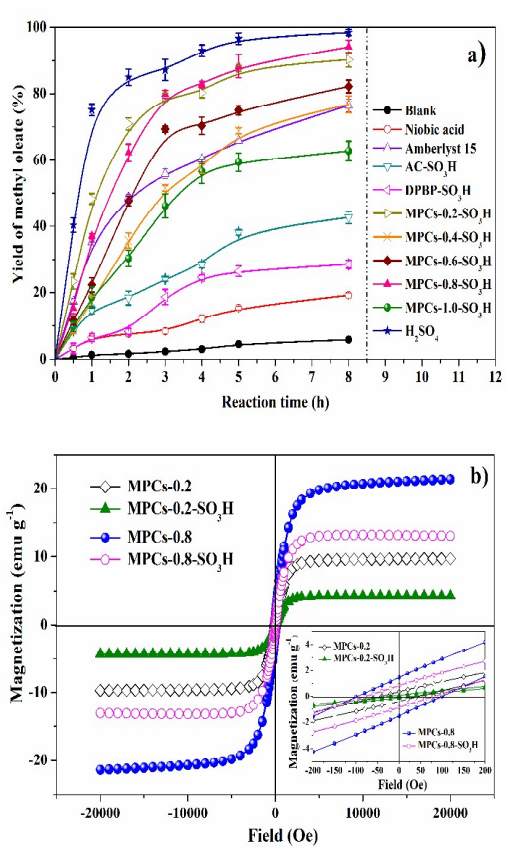

Fig. 5. Comparison of catalytic activities in conversion of OA and methanol, reaction conditions: acid catalyzed (150 mg catalyst) esterification of OA (150 mg) with methanol (5 g) at 80 °C (a); magnetization curves of the MPCs-0.2, MPCs-0.2-SO_3H, MPCs-0.8 and MPCs-0.8-SO_3H at room temperature (b). Insert: enlargement of the -200 to 200 Oe region

RSC Advances

ARTICLE

Table 1. Catalytic activity of various solid acid catalysts for the esterification of OA and methanol. (Reaction conditions: weight ratio of OA to methanol 1:33, catalyst loading of 3 wt%, reaction temperature of 80 °C; reaction time for maximum yield and TOF were 8 and 2 h, respectively.)

Catalyst	Acid capacity [a]		Initial rate [b]	Conv.	TOF
	(mmol H^+ g^{-1})	(10^{-3} mmol H^+ m^{-2})	(10^{-2} mmol g^{-1} min^{-1})	(8h, %)	(10^{-3} min^{-1})
MPCs-0.2-SO_3H	1.79	11.5	1.99	90	1.58
MPCs-0.4-SO_3H	1.83	10.6	1.00	77	0.82
MPCs-0.6-SO_3H	2.47	2.3	1.33	82	0.81
MPCs-0.8-SO_3H	2.68	2.2	1.75	94	0.98
MPCs-1.0-SO_3H	1.43	2.3	1.19	63	0.88
DPBP-SO_3H	0.58	7.3	0.40	27	0.58
AC-SO_3H	1.02	1.8	0.52	43	0.76
Amberlyst-15	4.7	104.4	1.37	76	0.0026
Niobic acid ($Nb_2O_5 \cdot nH_2O$)	0.32	2.5	0.21	19	0.0009

[a] Calculated by titration experiment. [b] Reaction condition: acid catalyzed (150 mg catalyst) esterification of OA (150 mg) with methanol (5 g) at 80 °C for 2 h.

3.4 Kinetics of acid catalyzed esterification of OA

The kinetic parameters for esterification reaction were determined using Arrhenius equation (see the supporting information). Results indicate that the reaction rate constant obtained with the MPC-*x*-SO_3H catalysts are significantly higher than that obtained with Amberlyst-15 (Table S2, Fig. S21). The activation energies range from 26 to 36 KJ mol^{-1}. These values are lower than those for Amberlyst-15 and other reported solid acids.[31,32] The present catalysts are therefore promising candidates for use in esterification, because their activities are comparable to those of mineral acids and higher than those of other solid acids.

3.5 Water tolerance

Water tolerances of MPC-0.2-SO_3H, MPC-0.4-SO_3H, MPC-0.6-SO_3H, and MPC-0.8-SO_3H were compared with that of Amberlyst-15 in esterification of OA and methanol. The initial rates and TOFs of the four as-prepared catalysts slowly decreased linearly with increasing addition of up to 5.0 wt% water to the feedstock. In contrast, the initial rate and TOF of Amberlyst-15 sharply decreased on addition of up to 1.0 wt% water to the feedstock (Fig. S22). This is because the acid strength of the catalyst is decreased by the formation of hydration spheres around the sulfonic acid groups. Furthermore, water increases the polarity around the acid moieties, and this hinders access of hydrophobic long-chain carboxylic acids. The acid strength of the phenylsulfonic acids in Amberlyst-15 is higher than those of the MPC-*x*-SO_3H materials; i.e., Amberlyst-15 has a higher water-absorption capacity than MPC-*x*-SO_3H. The as-prepared catalysts contain nitrogen atoms in the forms of pyridine, quaternary nitrogen, pyrroles, and pyridine *N*-oxide (Fig. S12b) and -COOH, and these easily form hydrogen bonds with water, further decreasing the initial rates and TOFs. Although the presence of water lowers the activities of MPC-*x*-SO_3H and Amberlyst 15, the MPC-*x*-SO_3H catalysts, which have high surface areas and pore volumes, have better water tolerance than Amberlyst-15 in esterification.

Additionally, the sulfonated carbon (e.g., MPCs-0.8-SO_3H, acid capacity: 2.68 mmol H^+ g^{-1}, 0.5 g) was dispersed in deionized water (50 mL) and the solution was stirred at 95 °C for 5 h. After removing the catalyst by filtration, the filtrate was titrated using a pH meter and standardized 0.01 mol L^{-1} NaOH solution. From the amount of the NaOH solution consumed, the amount of acid groups leached from the MPCs-0.8-SO_3H was calculated to be 19.8 % relative to the initial acid groups. Compared with previous result (26%–29%),[7b] it can be seen that the as-made MPCs-0.8-SO_3H has moderate stability under the same hydrolytic conditions.

3.6 Reusability and isolation of catalysts

The yields of methyl oleate and the TOFs for MPC-*x*-SO_3H (*x* = 0.2, 0.4, 0.6, 0.8) slowly declined after four cycles, whereas the catalytic activity of Amberlyst 15 sharply decreased after the first run (Fig. S23). The good recyclability of MPC-*x*-SO_3H is attributed to the high stability of porous carbon and strong attachment of sulfonic acid groups to the substrate. Representative XPS results for the fresh MPC-0.8-SO_3H catalyst and the catalyst after four cycles (Fig. S24) showed that there were no obvious changes in the surface element contents of C, O, S, and Fe; this indicates the high stability of MPC-0.8-SO_3H in esterification.

Catalyst isolation is an important factor in practical

applications.[10] The magnetic hysteresis curves of the samples showed nonlinear and reversible behavior, with superparamagnetism (Fig. 5b). The saturation magnetizations of MPC-0.2, MPC-0.2-SO_3H, MPC-0.8, and MPC-0.8-SO_3H are 9.71, 4.28, 21.42, and 13.07 emu g^{-1}, respectively, which are sufficient for separation of the particles by an external magnetic field (Fig. S25).

To the best of our knowledge, this is the first report of the synthesis of magnetic CSAs from waste BP via a facile tactics for the esterification of oleic acid. The good catalytic activities of MPC-0.2-SO_3H and MPC-0.8-SO_3H are attributed to their synergetic combination of the unique porous carbon structure and three functional groups (-SO_3H, -COOH, and phenolic OH groups) in adequate amounts. Researchers have also proved that sulfonated-ACs contain phenolic-OH, –COOH, and –SO_3H groups and therefore exhibit better catalytic activity during liquid-phase acid-catalyzed reactions compared to other solid acids.[4,13] Furthermore, the hybrid Fe_3O_4 nanocrystalline enable easy separation of the catalysts from the reaction mixtures, so the catalysts meet the demands of environmental protection. The materials presented here therefore have great potential as stable and highly active CSAs (Table S3).

4. Conclusions

Magnetically carbonaceous solid acids with variable surface areas and pore volumes were fabricated by using a facie strategy from BP. High acid densities and hydrophobic surface properties of the as-obtained magnetic CSAs make them highly efficient catalysts for biodiesel production. The large pores favor the diffusion of large organic molecules, contributing to enhancement of catalytic ability. Results show that these materials have better catalytic properties than Amberlyst-15. Their excellent magnetic separation abilities make the production more convenient and robust. These findings offer a new pathway to the fabrication of magnetic CSAs and develop a holistic approach to biomass conversion and environmental protection.

Acknowledgements

This project was supported by the National Natural Science Foundation of China (21275098), and National Undergraduate Innovation Program of China (201410718010).

Notes and references

1 F. Su and Y. Guo, *Green Chem*., 2014, **16**, 2934-2957.
2 Zillillah, G. Tan and Z. Li, *Green Chem*., 2012, **14**, 3077-3086.
3 C. Poonjarernsilp, N. Sano and H. Tamon, *Appl. Catal. B-Environ*., 2014, **147**, 726-732.
4 L.J. Konwar, J. Boro and D. Deka, *Renew. Sustain. Energy Rev*., 2014, **29**, 546-564.
5 A. Sivasamy, K.Y. Cheah, P. Fornasiero, F. Kemausuor, S. Zinoviev and S. Mietus, *ChemSusChem*, 2009, **2**, 278-300.
6 a) Zillillah, T.A. Ngu and Z. Li, *Green Chem*., 2014, **16**, 1202-1210; b) G. Xiao, J. Zhou, X. Huang, X. Liao and B. Shi, *RSC Adv*., 2014, **4**, 4010-4019.
7 a) S.-Y. Chen, T. Yokoi, C.-Y. Tang, L.-Y. Jang, T. Tatsumi, J.C.C. Chan and S. Cheng, *Green Chem*., 2011, **13**, 2920-2930; b) D. Lee, *Molecules*, 2013, **18**, 8168-8180; c) F. Liu, J. Sun, Q. Sun, L. Zhu, L. Wang, X. Meng, C. Qi and F.-S. Xiao, *Catal. Today*, 2012, **186**, 115-120; d) V. Mirkhani, M. Moghadam, S. Tangestaninejad, I. Mohammadpoor-Baltork and M. Mahdavi, *J. Iran. Chem. Soc*., 2011, **8**, 608-615.
8 a) X. Duan, Y. Liu, Q. Zhao, X. Wang and S. Li, *RSC Adv*., 2013, **3**, 13748-13755; b) Y. Zhao, H. Wang, Y. Zhao and J. Shen, *Catal. Comm*., 2010, **11**, 824-828; c) X.-Y. Liu, M. Huang, H.-L. Ma, Z.-Q. Zhang, J.-M. Gao, Y.-L. Zhu, X.-J. Han and X.-Y. Guo, *Molecules*, 2010, **15**, 7188-7196; d) M. Kitano, K. Arai, A. Kodama, T. Kousaka, K. Nakajima, S. Hayashi and M. Hara, *Catal Lett*., 2009, **131**, 242-249; e) X. Liang and J. Yang, *Catal Lett*., 2009, **132**, 460-463.
9 W.-J. Liu, K. Tian, H. Jiang and H.-Q. Yu, *Sci. Rep*., 2013, **3**, 2419.
10 F.-C. Zheng, Q.-W. Chen, L. Hu, N. Yan and X.-K. Kong, *Dalton Trans*., 2014, **43**, 1220-1227.
11 J. Safari and Z. Zarnegar, Ultrason. Sonochem., 2013, **20**, 740-746.
12 Z. Gao, S. Tang, X. Cui, S. Tian and M. Zhang, *Fuel*, 2015, **140**, 669-676.
13 H. Ma, J. Li, W. Liu, B. Cheng, X. Cao, J. Mao and S. Zhu, *J. Agric. Food Chem*., 2014, **62**, 5345-5353.
14 C.R. Silva, T.F. Gomes, G.C.R. M. Andrade, S.H. Monteiro, A.C.R. Dias, E.A.G. Zagatto and V.L. Tornisielo, *J. Agric. Food Chem*., 2013, **61**, 2358-2363.
15 R.-L. Liu, F.-Y. Yin, J.-F. Zhang, J. Zhang and Z.-Q. Zhang, *RSC Adv*., 2014, **4**, 21465-21470.
16 G.W. Huber, S. Iborra and A. Corma, *Chem Rev*., 2006, **106**, 4044-4098.
17 M. Okamura, A. Takagaki, M. Toda, J.N. Kondo, K. Domen, T. Tatsumi, M. Hara and S. Hayashi, *Chem. Mater*., 2006, **18**, 3039-3045.
18 C. He, S. Wu, N. Zhao, C. Shi, E. Liu and J. Li, *ACS Nano*, 2013, **7**, 4459-4469.
19 J. Ji, G. Zhang, H. Chen, S. Wang, G. Zhang, F. Zhang and X. Fan, *Chem. Sci*., 2011, **2**, 484-487.
20 R.-L. Liu, W.-J. Ji, T. He, Z.-Q. Zhang, J. Zhang and F.-Q.Dang, *Carbon*, 2014, **76**, 84-95.
21 S.-F. Lim, Y.-M. Zheng, S.-W. Zou and J.P. Chen, *Environ. Sci. Technol*., 2008, **42**, 2551-2556.
22 M. Toupin and D. Belanger, *Langmuir*, 2008, **24**, 1910-1917.
23 K. Nakajima and M. Hara, *ACS Catal*., 2012, **2**, 1296-1304.
24 G. Wang, X. Zhang, A. Skallberg, Y. Liu, Z. Hu, X. Mei and K. Uvdal, *Nanoscale*, 2014, **6**, 2953-2963.
25 J.-D. Xiao, L.-G. Qiu, X. Jiang, Y.-J. Zhu, S. Ye and X. Jiang, *Carbon*, 2013, **59**, 372-382.
26 A. Banerjee, R. Gokhale, S. Bhatnagar, J. Jog, M. Bhardwaj, B. Lefez, B. Hannoyer and S. Ogale, *J. Mater. Chem*., 2012, **22**, 19694-19699.
27 S. Zhang, M. Zeng, J. Li, J. Li, J. Xu and X. Wang, *J. Mater. Chem. A*, 2014, **2**, 4391-4397.
28 R. Liu, X. Wang, X. Zhao and P. Feng, *Carbon*, 2008, **46**, 1664-1669.
29 X. Liang, *Chem. Eng. J*., 2015, **264**, 251-257.
30 Z.J. Chen, Z.H. Guan, M.R. Li, Q.H. Yang and C. Li, *Angew. Chem. Int. Ed*., 2011, **50**, 4913-4917.
31 S.S. Vieira, Z.M. Magriotis, N.A.V. Santos, A.A. Saczk, C.E. Hori and P.A. Arroyo, *Bioresource Technol*., 2013, **133**, 248-255.
32 A. Alegria, A.L. Fuentes de Arriba, J.R. Moran and J. Cuellar, *Appl. Catal. B-Environ*., 2014, **160-161**, 743-756.

Table of content entry

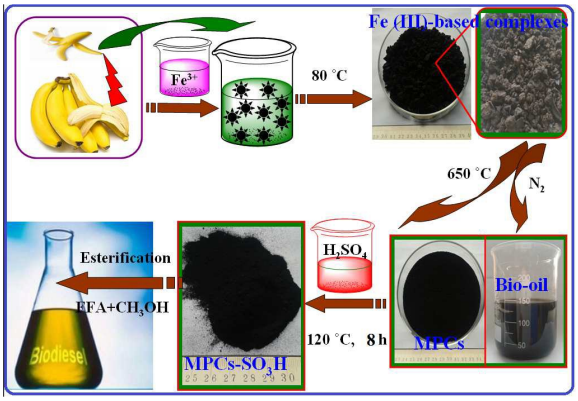

A kind of magnetically carbonaceous solid acids with high catalytic activities were fabricated from banana peel and were succesfully used for the esterification of oleic acid.